Journal of The Electrochemical Society, **161** (9) A1218-A1223 (2014)
0013-4651/2014/161(9)/A1218/6/$31.00 © The Electrochemical Society

Molecular Dynamics Simulations of the Traction-Separation Response at the Interface between PVDF Binder and Graphite in the Electrode of Li-Ion Batteries

Seungjun Lee,[a,c] Jonghyun Park,[a] Jun Yang,[b] and Wei Lu[a,z]

[a]*Department of Mechanical Engineering, University of Michigan, Ann Arbor, Michigan 48109, USA*
[b]*School of Chemistry & Chemical Engineering, Shanghai Jiao Tong University, Shanghai 200240, People's Republic of China*

Fracture in Li-ion battery electrodes is one of the main degradation mechanisms that limit the battery performance and lifetime. Debonding between the active and binder materials damages mechanical integrity, which leads to the loss of active materials and increased resistance. In this work, molecular dynamics (MD) simulation is used to evaluate the strength of the connectivity between polyvinylindene fluoride (PVDF) binder and graphite in the opening and sliding modes. The simulations revealed detailed failure behaviors at the atomistic scale. We have found that the separation occurs at the interface rather than inside the bulk materials, suggesting that the mechanical strength at the interface between PVDF binder and graphite is weaker than that of PVDF or graphite. Therefore, debonding at the interface is critical to the mechanical integrity of the electrode. Our calculations have provided quantitative traction-separation curves, and identified the maximum stresses of 300 MPa and 30 MPa for the normal and shear traction curves, respectively. The traction-separation curves obtained from the MD simulations will provide the critical input for the continuum level cohesive zone model to further study the inter-particle crack propagation in the electrode.
 [DOI: 10.1149/2.0051409jes]

Manuscript submitted March 5, 2014; revised manuscript received April 14, 2014. Published May 22, 2014.

Fracture of the electrode material is one of the main degradation mechanisms in Li-ion batteries,[1–4] which causes the loss of electric contact as well as enhances side reactions such as solid electrolyte interface (SEI) formation and dissolution due to the generation of new interfaces. The electrode fracture may occur at various size scales, including crystals, polycrystals, and aggregates.[5] Intercalation-induced deformation in active particles builds a stress field in the crystalline particles and can initiate crack formation. Moreover, the deformation confined by the mismatch of lattice orientation can induce cracks at grain boundaries. In addition to particle interiors, the deformation of active particles can cause fracture at the level of aggregates such as the debonding of binder and particles. The debonding failure of the constituent materials of the electrode is complicated because the electrode is a mixture of several components with different sizes and properties. It is important to understand the interfacial interactions inside the constituent materials in order to mitigate the undesirable failure.

Several theoretical studies have addressed crack problems in the battery system, but most of them have focused on a single particle.[3,6–8] For the study of inter-particle crack problems, the cohesive zone model (CZM) is an effective tool since it includes an intrinsic fracture energy dissipation mechanism while the classical continuum-based fracture analysis encounters the problem of stress singularity at the crack tip. CZM has been widely used to model delamination and debonding of composite structures.[9–12] In CZM, the fracture process is governed by the traction-separation law, which describes the relationship between cohesive traction and separation displacement at the crack tip. It is difficult to discern the traction-separation law directly by experiments because the level of traction typically ranges from hundreds of megapascals to gigapascals; on the other hand, the separation displacements are on the order of nanoscales. Atomistic simulations are useful for capturing fracture behaviors at such small size scales. The stress-strain responses from atomistic simulations can be parameterized to provide the traction-separation curves for CZM.

Several studies have used molecular dynamics (MD) simulations to investigate the traction-separation responses at an interface. For example, the stress-strain responses have been studied at the grain boundary of copper[13] and aluminum.[14] The interface of bi-material systems has been simulated for two BCC materials,[15,16] the FCC aluminum-silicon carbide system,[17] the aluminum-aluminum oxide system[18] and the graphene-polyethylene system.[19] These studies are motivated by the increasing interests on the mechanical behaviors at the interface of composite materials, which play an important role in the overall properties of new materials.

In a battery, the inter-particle mechanical strength plays an important role in maintaining the mechanical integrity of the composite electrode. However, the adhesion strengths at the interfaces of binder/active particle and active particle/binder/current collector have not been well studied, especially in comparison to the amount of work available on the mechanical strength of active particles. Recent researches have shown that the adhesion strength between active particles and binders strongly affects the electrical conductivity in composite electrodes[20] and the capacity retention.[21] Moreover, the role of binders becomes more important for high capacity active materials such as Si and Sn, which show a large volume change during charge/discharge cycles. For example, although Si microparticles do not undergo fracture during cycling, significant capacity loss occurs due to the loss of electric contact between particles, which can be prevented by enhancing the adhesion of binders.[22]

In this work, we aim to study the mechanical behavior at the interface of graphite and polyvinylindene fluoride (PVDF) binder using MD simulations. Graphite and PVDF are commonly used as anode particles and binders in the current commercial batteries. The stress-strain responses from MD simulations will be parameterized to obtain the traction-separation curves, which can further serve as inputs for CZM to investigate the inter-particle mechanical failure such as debonding between particles and binders in the electrode. This paper is structured as follows. First, the MD simulation methods and the potentials are described. For validation of the potentials, the calculated PVDF density and the wetting angle of PVDF on the graphite surface are compared with experiments. Next, the simulation results are shown for the opening and the sliding modes. Finally, the conclusion is given at the end.

Method

Description of the potentials.— For the PVDF binder, we use the classical potential functions and parameters developed by Oleksiy et al.[23] The van der Waals force and electrostatic energy are considered for non-bonding interactions. The stretching, bending and torsional energy are considered for covalent bond interactions. All the PVDF chains in this study consist of 20 repeating units of (-[CH_2-CF_2]-), and each end is terminated by -CH_3 and -CF_3, respectively. To validate the potential, we have calculated the density of PVDF. Initially, 20 PVDF chains are placed in parallel in a large system box. The system box is gradually shrunk with discrete steps until the volume becomes smaller

[c]Present address: Department of Mechanical, Robotics and Energy Engineering, Dongguk University-Seoul, 100715 Seoul, Korea.
[z]E-mail: weilu@umich.edu

than the expected value, which results in a higher density. At each step, the volume is kept the same with the NVT ensemble. Next, the system is switched to the NPT ensemble to calculate the relaxed volume at the atmospheric pressure. The system is annealed by increasing the temperature to 500 K and then decreasing the temperature to 300 K. By calculating the equilibrated system size, the density is obtained as 1.55 g/cm^3. This value is slightly lower than the known experimental value due to the small molecular weight of the simulated PVDF.[23] After scaling up the number of backbone carbons to the experimental data (simulation: 42 carbons, experiment: 1000 carbons), we obtain a density of 1.62 g/cm^3. This value is within 2% difference from the experiment density of 1.65 g/cm^3 at room temperature.[23] The agreement confirms the reliability of the potentials used in this work.

The Adaptive Intermolecular Reactive Empirical Bond Order (AIREBO) potential has been widely used for the graphite material.[24–26] This potential is expanded from the second generation REBO potential[27] by adding a Lennard Johnes (LJ) potential term and a torsional term. The LJ term in AIREBO potential enables the interlayer interaction of graphite.[26] In this work we adopt the AIREBO potential for graphite.

We account for the interaction between graphite and PVDF with the van der Waals force. The LJ form has been widely used to describe interfacial interactions.[24,28] The LJ parameters for the interaction between graphite and PVDF are calculated by the Lorentz-Berthelot mixing rule without developing additional potentials for the interaction. Following this rule, the values in the LJ potential between A and B atoms are calculated by the arithmetic mean for the zero potential distance, $\sigma_{AB} = (\sigma_{AA} + \sigma_{BB})/2$, and the geometric mean for the depth of the potential well, $\varepsilon_{AB} = \sqrt{\varepsilon_{AA}\varepsilon_{BB}}$, respectively.

To use the mixing rule for two atoms, the functional form of their potentials should be the same. Thus the Buckingham potential for PVDF is fitted to the LJ potential and the corresponding values of σ and ε are obtained from the curve fitting. In the system, six types of atoms are used to describe PVDF: -H, -F, and four types of carbons -C_{H2}-, -C_{F2}-, -C_{H3}, and -C_{F3}, while another type of carbon is used to describe graphite. Therefore, six types of interactions between PVDF and graphite should be defined and all of them are calculated by the Lorentz-Berthelot mixing rule. Representative potentials for carbons in PVDF and carbons in graphite are shown in Fig. 1.

To provide an additional validation, we have calculated the contact angle of PVDF binder on the graphite surface by simulations and compared it with the experimental measurement. The contact angle is calculated using a slab model[29] in our simulation, with the work of separation, W_{sep}, given by

$$W_{sep} = \sigma_{pvdf} + \sigma_{graphite} - \sigma_{pvdf/graphite} = (E_{pvdf-slab} + E_{graphite-slab} - E_{pvdf/graphite-slab})/A. \quad [1]$$

Here σ_{pvdf} and $\sigma_{graphite}$ are the surface energies of PVDF and graphite, respectively, and $\sigma_{pvdf/graphite}$ is the interfacial energy between PVDF and graphite; $E_{pvdf-slab}$, $E_{graphite-slab}$ and $E_{pvdf/graphite-slab}$ are the total energies of the PVDF, graphite and PVDF/graphite slab, respectively, and A is the interfacial area. The Young's equation gives the following relation between the contact angle and the surface energies,

$$\sigma_{pvdf}\cos\theta + \sigma_{pvdf/graphite} = \sigma_{graphite}, \quad [2]$$

where θ is the contact angle. With Eqs. 1 and 2, the work of separation, W_{sep}, can be written in terms of the contact angle, θ, as

$$W_{sep} = \sigma_{pvdf}(\cos\theta + 1). \quad [3]$$

Following Eqs. 1 and 3, the contact angle can finally be expressed as

$$\theta = \cos^{-1}\left(\frac{E_{pvdf-slab} + E_{graphite-slab} - E_{pvdf/graphite-slab}}{A\sigma_{pvdf}} - 1\right). \quad [4]$$

Each slab model is constructed as a stack of vacuum/slab/vacuum in the z direction. Periodic boundary conditions are used in the lateral directions. In the simulations, 30 PVDF chains and 4 layers of graphite are used. The total energies of the slab models are obtained after the system is equilibrated, which give $E_{pvdf-slab} = 2675.9$ eV, $E_{graphite-slab} = -14257.3$ eV and $E_{pvdf/graphite-slab} = -11586.3$ eV. The interfacial area A is 1244 Å^2. With $\sigma_{pvdf} = 34.1$ mJ/m^2 being the surface energy of PVDF,[30] the contact angle θ is calculated as 32°. To validate the simulation, we have used atomic force microscopy (AFM) to measure the contact angle of PVDF on the flat basal plane of Highly Ordered Pyrolytic Graphite (HOPG). The PVDF powder was melted on the HOPG surface to form a droplet, and then cooled down for AFM imaging and cross-section analysis. Figure 2 shows a representative AFM image. The contact angle is measured as 33°. The agreement between the computed and experimental values confirms the potentials and parameters used in the simulation.

MD model and simulation.— A representative MD model is shown in Fig. 3. The system consists of PVDF chains and four layers of graphite in an ABAB stacking form. Periodic boundary conditions are used in the x and y directions. Five different system sizes are simulated to determine the minimum volume size that can provide the representative cohesive zone parameters. The system size is determined by the number of PVDF chains, as summarized in Table I. The calculations are based on the assumption that the PVDF density is independent of the system size. We keep the molecular weight of a PVDF chain to be same as that in the density calculation. It is challenging to model large polymer chains in a bulk with MD, so our simulations represent the behavior of PVDF with small size of chains. However, we suspect that the effect of chain size on the cohesive

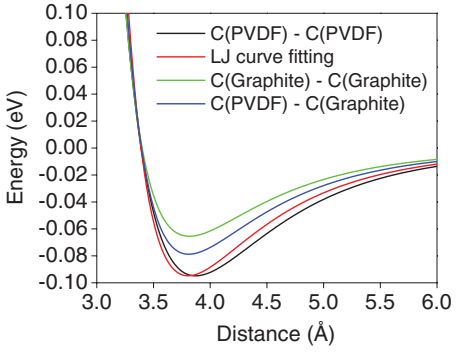

Figure 1. (Color online) Potentials for pair interactions between carbons in PVDF (shown here as example is the -C_{H2}- type of carbon in PVDF) and graphite.

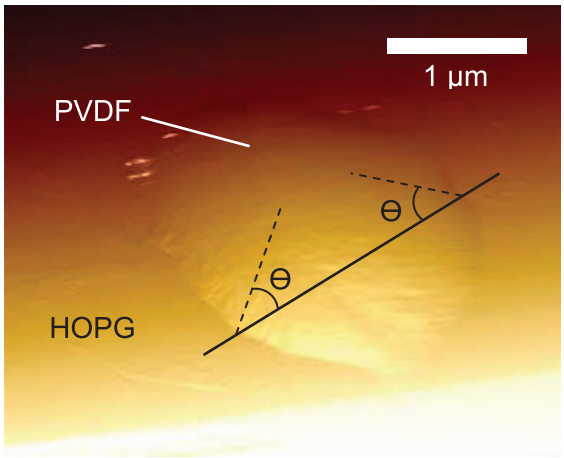

Figure 2. (Color online) AFM image of melted PVDF on the basal plane of HOPG.

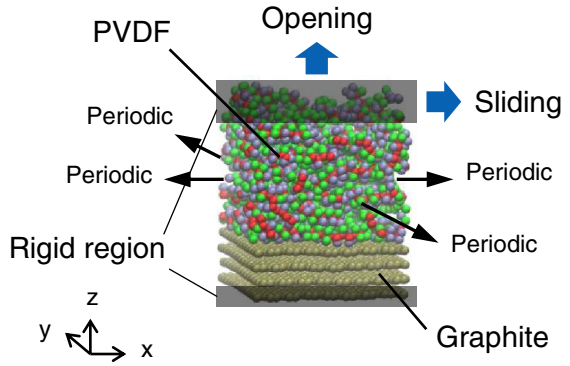

Figure 3. (Color online) A representative model for the MD simulation. Red: carbon atom; Green: fluoride atom; Purple: hydrogen atom.

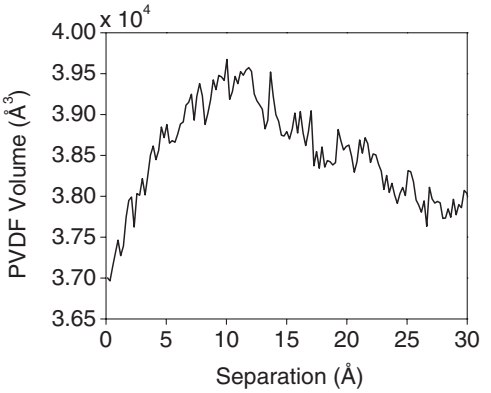

Figure 4. The volume change of PVDF as a function of separation (30 PVDF chains in the opening mode).

Table I. Cases of different system sizes in MD simulations.

Case	Number of PVDF chains	Size of one side (Å)	Area of graphite basal plane (Å^2)
1	5	19.4	376.8
2	10	24.5	598.1
3	20	30.8	949.4
4	30	35.3	1244.0
5	40	38.8	1507.0

strength is small since the separation is dominated by the process at the interface between PVDF and graphite.

All MD simulations are performed by the open source program LAMMPS,[31] which we have used in several calculations.[32–34] Initially, all PVDF chains are vertically placed above the graphite. As the simulation begins, the chains are agglomerated and attracted to the graphite surface due to interactions. After the PVDF is attached on the surface, the system is heated to 525 K, which is above the PVDF melting point to remove any initial artificial alignment. Then, the system is cooled down to 300 K and relaxed until it reaches equilibrium. A time step of 1 femtosecond is used in all simulations. The Nose-Hoover thermostat and Nose-Hoover barostat are used in all simulations with temperature damping constant of 0.1 picosecond and pressure damping constant of 1 picosecond. The equilibrium simulation is performed with the NPT ensemble at a pressure of 1 bar.

After equilibration, the atoms at the top of the PVDF and at the bottom of the graphite are constrained to serve as boundaries, while a tensile (mode I: opening mode) or a shear (mode II: sliding mode) load is applied on the top boundary. The bottom layer of the graphite is fixed in all directions. In the opening mode, the boundary atoms at the top of the PVDF are constrained only in the z direction with a constant velocity. In the sliding mode, the top layer of the PVDF is fixed in the y and z directions and constrained in the x direction. The opening and sliding simulations are performed with the NVT ensemble. Generally speaking, a high loading rate will affect the exhibited cohesive strength. In our simulations the separation is performed at a rate of 0.2 Å/ps, which is within the typical range of values used in MD simulations.

Stresses are calculated in the form of the virial stress, which is expressed as[35]

$$\boldsymbol{\sigma}(\mathbf{r}) = \frac{1}{\Omega}\sum_i \left[-m_i \dot{\mathbf{u}}_i \otimes \dot{\mathbf{u}}_i + \frac{1}{2}\sum_{j \neq i} \mathbf{r}_{ij} \otimes \mathbf{f}_{ij} \right], \qquad [5]$$

where Ω is the total volume, m_i is the mass of atom i, $\dot{\mathbf{u}}_i$ is the time derivative of $\mathbf{u}_i$ which denotes the displacement vector of atom i relative to a reference position, $\otimes$ is the cross product, $\mathbf{r}_{ij} = \mathbf{r}_j - \mathbf{r}_i$ where $\mathbf{r}_i$ is the position vector of atom i, and $\mathbf{f}_{ij}$ is the interatomic force applied on atom i by atom j. The total volume Ω needs to be updated at each time step in the normal separation calculation because the system undergoes a large deformation accompanying the formation of irregular voids inside the PVDF polymer. To calculate the true volume of PVDF, we fill the simulation box with a lattice of imaginary small probe spheres, and then count the number of probe spheres that overlap with any atom in the PVDF. An overlap probe sphere indicates that the volume represented by it is occupied by PVDF. The ratio between the number of overlap probe spheres and the total number of probe spheres in the simulation box gives the volume fraction of PVDF in the simulation box. Therefore, the true volume of PVDF can be obtained by this volume fraction multiplied with the volume of the simulation box, which is known. To check overlapping, we use the atomic radius of each type of atoms in PVDF to define the boundary of an atom. A representative volume change for 30 PVDF chains in the opening mode is shown in Fig. 4. The volume increases at the initial stage as the system is stretched and shows a peak around the separation of 10 Å. The stress peak occurs at a separation of around 5 Å, so the volume peak happens at a larger separation. The reason for the mismatch of the volume peak and the stress peak is that fracture actually begins to occur just after 5 Å. There is a competition of disconnection due to fracture and the volume increase due to stretching. The former slows down the volume increase by relaxing the stress. Fracture starts to dominate after the separation reaches 10 Å. At this point voids begin to appear and grow continuously, relaxing the internal stresses inside PVDF and causing its volume to decrease. The final volume of PVDF is slightly different from the initial volume, and the difference can be reduced by decreasing the size of the probe spheres. However, the effect of this discrepancy is little because the difference is less than 3% in volume. Moreover, the numerator of the virial stress is already almost zero after the complete separation.

Results

Opening mode.— Figure 5a shows normal traction–separation responses of small size systems (5, 10 and 20 PVDF chains). The normal tractions (σ_{zz}) and the corresponding separations are averaged over 1ps to reduce the thermal oscillation. The separations are measured by the relative displacements of the top and bottom boundaries. The normal traction increases almost linearly at the beginning of the simulation, which corresponds to elastic deformation. The normal traction reaches a peak of around 0.25 GPa at a separation of 3–4 Å, then decreases continuously to zero at a separation of around 30 Å. The response shows a relatively large fluctuation due to small system sizes. The MD simulations exhibit similar separation behaviors for the three cases. The snapshots of 10 PVDF chains at different separation displacements are shown in Fig. 5b-5f. Initially, the PVDF is stretched without any fracture. The snapshot at a separation of 3 Å is almost the same as the initial configuration (Fig. 5b). After the normal traction reaches the maximum, debonding of the PVDF chains begins to occur.

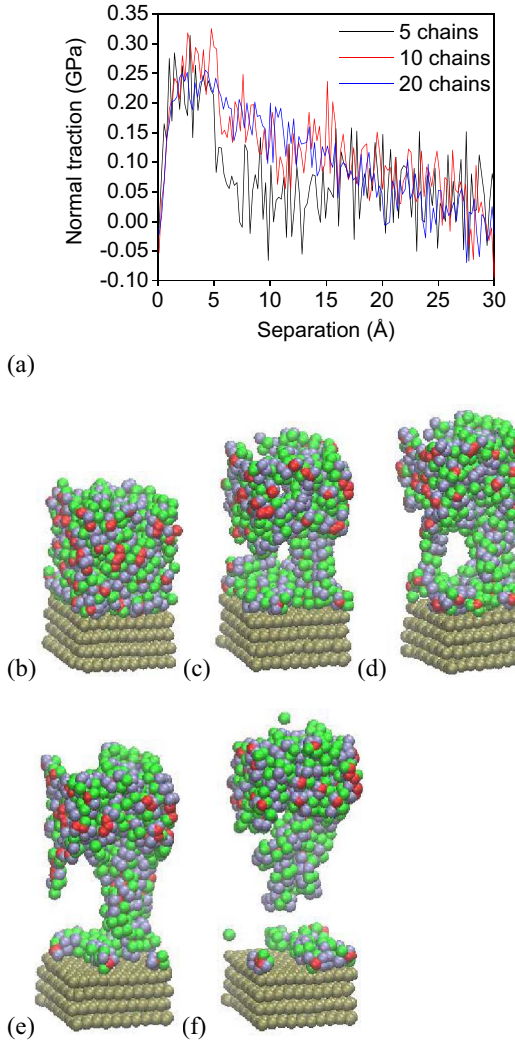

Figure 5. (Color online) (a) Normal traction-separation responses from MD simulations with 5, 10 and 20 PVDF chains. Also shown are snapshots of MD simulations with 10 PVDF chains and separation displacements of (b) 3 Å, (c) 12 Å, (d) 17 Å, (e) 22 Å and (f) 29 Å. Red: carbon atom; Green: fluoride atom; Purple: hydrogen atom.

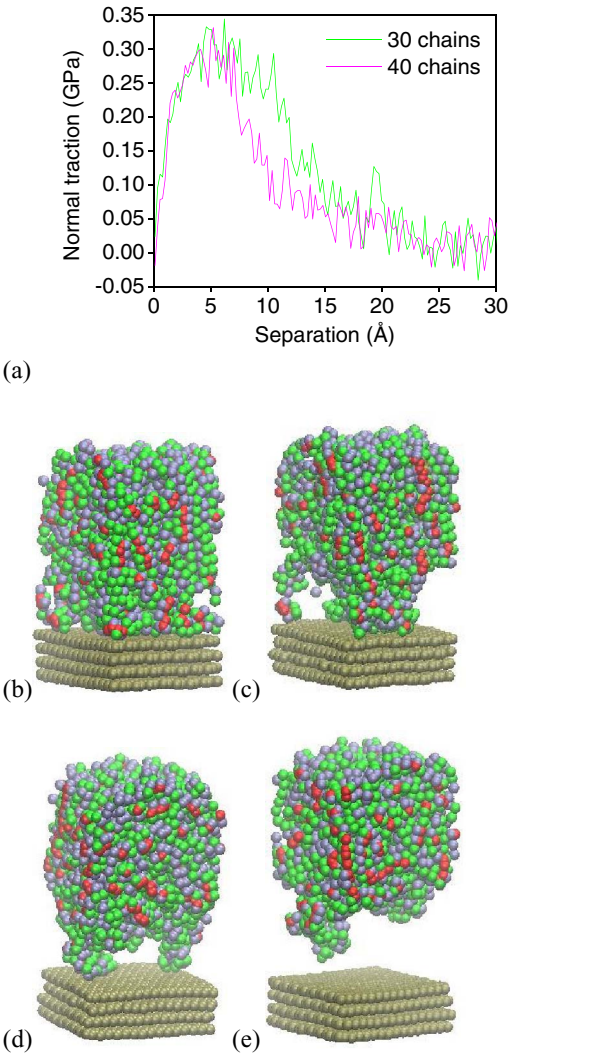

Figure 6. (Color online) (a) Normal traction-separation responses of MD simulations for 30 and 40 PVDF chains. Also shown are snapshots of MD simulations with 30 PVDF chains and separation displacements of (b) 10 Å, (c) 14 Å, (d) 17 Å and (e) 23 Å. Red: carbon atom; Green: fluoride atom; Purple: hydrogen atom.

A hole appears inside the PVDF at a separation of 12 Å, when the true volume reaches the maximum (Fig. 5c). The hole always emerges close to the interface regardless of the system size, which implies that the mechanical strength is weak near the interface. As the separation continues, the hole becomes larger (Fig. 5d) and a long PVDF column forms (Fig. 5e). Finally, the PVDF column breaks close to the PVDF/graphite interface, leaving some PVDF on the graphite surface (Fig. 5f). Although a small amount of PVDF may still remain on the graphite surface, the simulations show that the separation always occurs almost on the interface.

Figure 6a shows normal traction – separation responses of large size systems (30 and 40 PVDF chains). Compared to the smaller systems, the large systems show much smaller fluctuations in the curve. In general, as the system size increases, the maximum traction increases and the maximum separation decreases but the change is small. Eventually, the maximum traction converges to 0.3 GPa, and the maximum separation converges to 23 Å. Similar to what has been observed in the small systems, holes start to emerge near the interface with increasing separation (Fig. 6b). However, the holes appear to grow toward the interface rather than stay inside the PVDF (Fig. 6c). As the separation increases further, short PVDF columns emerge just above the interface (Fig. 6d), unlike the long columns observed in the small systems. These short columns hold up most of the PVDF on the graphite surface, resulting in no PVDF left on the graphite surface. Finally, a clean separation between the PVDF and the graphite is observed (Fig. 6e). The clean separation suggests that the interface is mechanically weaker than graphite or PVDF. Although in very small systems some PVDF may remain on the graphite surface, the separation can be treated to happen on the surface from a practical point of view. We suspect that the small systems are more constrained so that the chains cannot move around on the graphite surface as easily, leading to some residue on the surface.

The traction-separation response obtained by the MD simulations can be parameterized for a higher level continuum model such as CZM. The exponential cohesive zone model is derived using the following equation,

$$\sigma = \sigma_c \left(\frac{\delta}{\delta_c}\right) \exp\left(1 - \frac{\delta}{\delta_c}\right), \qquad [6]$$

where σ_c is the maximum traction and δ_c is the separation displacement at $\sigma = \sigma_c$.[36] Our simulations give $\sigma_c = 0.3$ GPa and $\delta_c = 5$ Å. The exponential traction–separation curve is shown in Fig. 7. In addition, the work of separation can be calculated by integrating Eq. 6 with respect to the separation displacement. The calculated work of

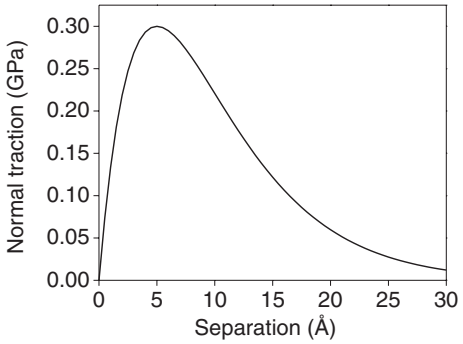

Figure 7. The traction-separation curve at the PVDF/graphite interface in the opening mode.

separation from our simulations is 0.4077 J/m^2. This value is higher than the work of separation for the polyester/graphite interface, which is about 0.2 J/m^2 from theoretical calculations,[37] suggesting that the PVDF/graphite interface is stronger. This value is less than 0.5 J/m^2, the work of separation for the graphite/graphite interface,[37] which is consistent with our MD simulations showing that the mechanical interaction at the interface is weaker than that in graphite.

Sliding mode.— In the sliding mode, the shear stress (σ_{xz}) is calculated as the top boundary atoms are moved in the x direction. It is expected that the shear responses of crystalline structures show a periodic pattern because a lattice shift results in the same configuration as before the shift. With the periodic conditions, no separation actually occurs because atoms that move out of the simulation box return to the opposite side. Non-periodic condition can be considered to estimate the separation response. However, the results will be strongly dependent on the simulation size if the system modeled is small such as in nanometers. In this study, we focus on the periodic conditions for the sliding mode.

First, sliding mode simulations are performed with a system size as small as possible, which consists of 5 PVDF chains and 2 layers of graphite for testing whether the predicted periodic shear responses can be obtained. For the test, all graphite atoms are fixed throughout the entire simulation in order to keep a perfect flat surface of the graphite crystalline structure. After equilibrium, all PVDF atoms are also fixed to prevent thermal fluctuation, after which the PVDF atoms are moved in the x direction. This simulation with all atoms frozen (no fluctuation) is performed as a validation of the sliding mode, and the shear stress should reflect the periodicity of graphite. Figure 8a shows the shear stress of the graphite atoms as a function of shear displacement, which gives a periodic pattern where the wavelength of the curve matches that of the graphite structure.

Next, sliding mode simulations are performed for case 4 in Table I, whose size is large enough to show convergence in the opening mode results. After 30 PVDF chains are equilibrated on the 4 layer graphite, the atoms at the top of the PVDF and the atoms at the bottom layer of the graphite are fixed to serve as boundaries, and then the top fixed atoms are moved in the x direction. The shear stress is shown in Fig. 8b. Compared to Fig. 8a, the response shows irregular oscillations with short wavelengths due to the movement of atoms in the PVDF and the graphite. The magnitude of the maximum shear stress does not exceed 0.03 GPa, which is one order smaller than the maximum normal stress in the opening mode.

Conclusions

In this study, MD simulations were performed to evaluate the traction-separation responses at the interface of PVDF binder and graphite active particles. Converged simulation results were obtained for the normal traction-separation responses by increasing the system sizes. The maximum normal traction in the opening mode is almost ten times of the maximum shear stress in the sliding mode. The information from MD simulations was used to extract parameters for

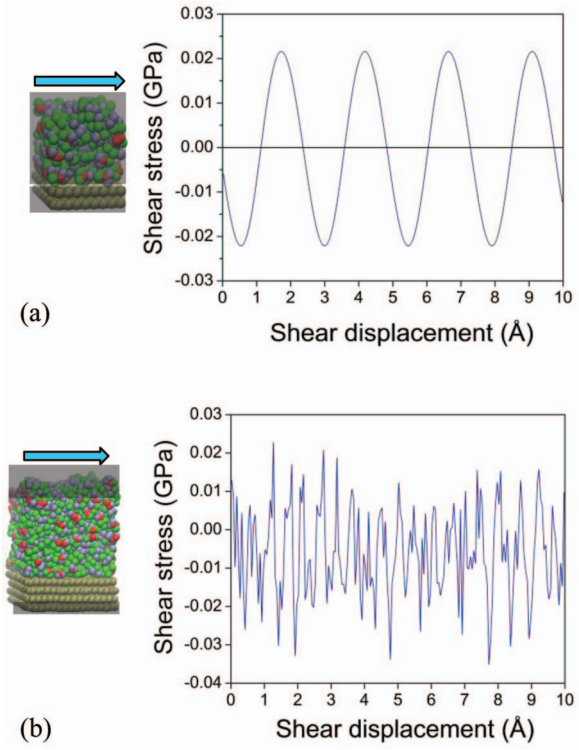

Figure 8. (Color online) Shear stress responses in the sliding mode. (a) shear response for an ideal case of fixed PVDF atoms moving all together on a flat graphite surface (5 PVDF chains and 2 atomic layers of graphite). (b) shear responses of 30 PVDF chains by moving the atoms at the top of the PVDF.

the continuum CZM. In addition to quantitative data, MD simulations show how the separation happens through void formation, and suggest that mechanical strength at the interface is weaker than that of graphite and PVDF binder. The computational framework can be used to study the stress responses of other systems such as the interface between the current collector and the composite electrode film, which is another important issue in the mechanical degradation of Li-ion batteries.

Acknowledgment

This research was funded by the GM /UM Advanced Battery Coalition for Drivetrains and the UM-SJTU collaborative research grant. Support from our sponsors is gratefully acknowledged.

References

1. R. A. Huggins and W. D. Nix, *Ionics*, **6**, 57 (2000).
2. D. Wang, X. Wu, Z. Wang, and L. Chen, *Journal of Power Sources*, **140**, 125 (2005).
3. M. Zhu, J. Park, and A. M. Sastry, *Journal of The Electrochemical Society*, **159**, A492 (2012).
4. H.-L. Zhang, F. Li, C. Liu, J. Tan, and H.-M. Cheng, *The Journal of Physical Chemistry B*, **109**, 22205 (2005).
5. Y. Hu, X. Zhao, and Z. Suo, *Journal of Materials Research*, **25**, 1007 (2010).
6. K. Zhao, M. Pharr, J. J. Vlassak, and Z. Suo, *Journal of Applied Physics*, **108**, 073517 (2010).
7. J. Christensen and J. Newman, *Journal of The Electrochemical Society*, **153**, A1019 (2006).
8. W. H. Woodford, Y.-M. Chiang, and W. C. Carter, *Journal of The Electrochemical Society*, **157**, A1052 (2010).
9. R. Borg, L. Nilsson, and K. Simonsson, *Composites Science and Technology*, **62**, 1299 (2002).
10. A. Turon, C. G. Dávila, P. P. Camanho, and J. Costa, *Engineering Fracture Mechanics*, **74**, 1665 (2007).
11. N. Chandra, H. Li, C. Shet, and H. Ghonem, *International Journal of Solids and Structures*, **39**, 2827 (2002).
12. S. Li, M. D. Thouless, A. M. Waas, J. A. Schroeder, and P. D. Zavattieri, *Composites Science and Technology*, **65**, 281 (2005).

13. D. E. Spearot, K. I. Jacob, and D. L. McDowell, *Mechanics of Materials*, **36**, 825 (2004).
14. V. Yamakov, E. Saether, D. R. Phillips, and E. H. Glaessgen, *Journal of the Mechanics and Physics of Solids*, **54**, 1899 (2006).
15. X. W. Zhou, J. A. Zimmerman, E. D. Reedy Jr, and N. R. Moody, *Mechanics of Materials*, **40**, 832 (2008).
16. X. W. Zhou, N. R. Moody, R. E. Jones, J. A. Zimmerman, and E. D. Reedy, *Acta Materialia*, **57**, 4671 (2009).
17. C. R. Dandekar and Y. C. Shin, *Composites Part A: Applied Science and Manufacturing*, **42**, 355 (2011).
18. C. R. Dandekar and Y. C. Shin, *Composites Science and Technology*, **71**, 350 (2011).
19. P. A. Amnaya, C. L. Dimitris, and C. H. Daniel, *Modelling and Simulation in Materials Science and Engineering*, **17**, 015002 (2009).
20. G. Liu, H. Zheng, A. S. Simens, A. M. Minor, X. Song, and V. S. Battaglia, *Journal of The Electrochemical Society*, **154**, A1129 (2007).
21. J.-H. Lee, U. Paik, V. A. Hackley, and Y.-M. Choi, *Journal of Power Sources*, **161**, 612 (2006).
22. Z. Chen, L. Christensen, and J. R. Dahn, *Journal of The Electrochemical Society*, **150**, A1073 (2003).
23. O. G. Byutner and G. D. Smith, *Macromolecules*, **33**, 4264 (2000).
24. M. Fuentes-Cabrera, B. H. Rhodes, J. D. Fowlkes, A. López-Benzanilla, H. Terrones, M. L. Simpson, and P. D. Rack, *Physical Review E*, **83**, 041603 (2011).
25. S. K. Pregler, T. Hayakawa, H. Yasumatsu, T. Kondow, and S. B. Sinnott, *Nuclear Instruments and Methods in Physics Research Section B: Beam Interactions with Materials and Atoms*, **262**, 240 (2007).
26. S. J. Stuart, A. B. Tutein, and J. A. Harrison, *The Journal of Chemical Physics*, **112**, 6472 (2000).
27. W. B. Donald, A. S. Olga, A. H. Judith, J. S. Steven, N. Boris, and B. S. Susan, *Journal of Physics: Condensed Matter*, **14**, 783 (2002).
28. S.-P. Huang, D. S. Mainardi, and P. B. Balbuena, *Surface Science*, **545**, 163 (2003).
29. Q. Zhang, T. Çağın, A. van Duin, W. A. Goddard III, Y. Qi, and L. G. Hector, Jr., *Physical Review B*, **69**, 045423 (2004).
30. D. Y. Kwok and A. W. Neumann, *Acid-Base Interactions: Relevance to Adhesion*, **2**, 91 (2000).
31. S. Plimpton, *Journal of Computational Physics*, **117**, 1 (1995).
32. S. Lee and W. Lu, *Applied Physics Letters*, **94**, 233114 (2009).
33. S. Lee and W. Lu, *Nanotechnology*, **22**, 205501 (2011).
34. S. Lee, J. Park, A. M. Sastry, and W. Lu, *Journal of The Electrochemical Society*, **160**, A968 (2013).
35. A. K. Subramaniyan and C. T. Sun, *International Journal of Solids and Structures*, **45**, 4340 (2008).
36. C.-T. Sun and Z. Jin, *Fracture Mechanics*, in, Academic Press (2011).
37. D. J. Henry, G. Yiapanis, E. Evans, and I. Yarovsky, *The Journal of Physical Chemistry B*, **109**, 17224 (2005).